Available online at www.sciencedirect.com
ScienceDirect
Corrosion Science xxx (2007) xxx–xxx
CORROSION SCIENCE
www.elsevier.com/locate/corsci

Corrosion inhibition using superhydrophobic films

Philip M. Barkhudarov [a], Pratik B. Shah [b,1], Erik B. Watkins [a,e], Dhaval A. Doshi [a,2], C. Jeffrey Brinker [b,c,d], Jaroslaw Majewski [a,*]

[a] Manuel Lujan Jr. Neutron Scattering Center, Los Alamos National Laboratory, MS-H805, Los Alamos, NM 87545, USA
[b] Center for Micro-Engineered Materials, University of New Mexico, Albuquerque, NM 87106, USA
[c] Sandia National Laboratories, Albuquerque, NM 87106, USA
[d] Utrecht University, 3508 TC Utrecht, The Netherlands
[e] University of California, Davis, CA 95616, USA

Received 30 August 2007; accepted 5 October 2007

Abstract

Neutron reflectivity (NR) was used to study the effectiveness of superhydrophobic (SH) films as corrosion inhibitors. A low-temperature, low-pressure technique was used to prepare a rough, highly porous organosilica aerogel-like film. UV/ozone treatments were used to control the surface coverage of hydrophobic organic ligands on the silica framework, allowing the contact angle with water to be continuously varied over the range of 160° (SH) to <10° (hydrophilic). Thin (~5000 Å) nano-porous films were layered onto aluminium surfaces and submerged in 5 wt% NaCl in D_2O. NR measurements were taken over time to observe interfacial changes in thickness, density, and roughness, and therefore monitor the corrosion of the metal. NR shows that the SH nature of the surface prevents infiltration of water into the porous SH film and thus limits the exposure of corrosive elements to the metal surface.

Keywords: A. Aluminium; A. Sputtered films; A. Organic coatings; B. Neutron reflectivity; C. Saltwater corrosion

1. Introduction

Recent discoveries have linked the mechanism for the self-cleaning of a lotus plant to a microscopic morphology leading to ultrahydrophobic surfaces (i.e. surface contact angle with water >150°). This finding has sparked the interest of numerous researchers to develop a biomimetic approach to producing the same effect. The prospect of producing surfaces that repel water suggests huge opportunities in the area of corrosion inhibition for metal components, chemical and biological agent protection for clothing, antifouling for marine vehicles, among many other applications. Different approaches have been successful at achieving very hydrophobic character of surfaces by various methods resulting from purposeful surface modification. Although successful at producing water repelling surfaces, these approaches have generally been only of academic interest due to complexity, cost, and lack of applicability to practical uses. The University of New Mexico (UNM) has teamed with Luna Innovations to develop superhydrophobic (SH) coatings that are simple to apply using conventional techniques, and will be cost effective for widespread use in various commercial applications.

This research focused on aluminium corrosion. In dry, non-salty environments aluminium develops a thin aluminium oxide layer (on the order of 20 Å), which inhibits further corrosion. However, in wet, salty environments, this oxide layer is penetrated, and further corrosion ensues, producing more oxide. Given their strong water repulsive properties, SH coatings are an ideal candidate for slowing the breakdown of the native aluminium oxide layer and thereby slowing corrosion of the aluminium layer underneath.

* Corresponding author. Tel.: +1 505 667 8840; fax: +1 505 665 2676.
E-mail address: jarek@lanl.gov (J. Majewski).
[1] Currently at Luna Innovations, VA 24073, USA.
[2] Currently at Cabot Corporation, MA 01821, USA.

0010-938X/$ - see front matter © 2007 Published by Elsevier Ltd.
doi:10.1016/j.corsci.2007.10.005

2. Superhydrophobic surfaces

We all can recall seeing water droplets "bead up" on the leaves of plants. Most famous is the Lotus leaf, called the "symbol of purity", because of its self-cleaning properties. At very shallow angles of inclination or with the slightest wind, water droplets roll rather than flow [1,2]. The rolling droplets entrain particle contaminants and parasites, thereby cleaning them from the Lotus leaf surface. It is now recognized that the fascinating fluid behaviors observed for the Lotus plant, like the rolling and bouncing of liquid droplets and self-cleaning of particle contaminants, arise from a combination of the low interfacial energy and the rough surface topography of waxy deposits covering their leaves [3].

Phenomenologically, Cassie and Baxter postulated that the cosine of the contact angle on a heterogeneous solid/air surface is the sum of the cosine of the contact angles of the respective homogeneous surfaces weighted by the surface fraction of the solid [4,5], $\cos\theta^{\alpha} = -1 + \Phi_S(1 + \cos\theta)$, where θ^{α} is the apparent contact angle, -1 is the cosine of the contact angle of the air surface, and Φ_S is the surface fraction of solid. As the ratio of the pillar width to interpillar distance of a regular lithographically defined surface decreases [6] or the roughness of a random, porous (e.g. fractal) surface increases, Φ_S approaches zero, and θ^{α} approaches 180°. Interestingly, Herminghaus postulates that hierarchical roughness could render any surface (independent of microscopic contact angle) superhydrophobic [7], but this has not yet been observed. Wenzel has put forward a different relationship for contact angles on rough surfaces [8]: $\cos\theta^{\alpha} = r\cos\theta$, where r is the roughness parameter defined by the ratio of the real surface area to the projected surface area. Because $r \geqslant 1$, roughness on a hydrophobic surface ($\theta > 90°$) renders it more hydrophobic, whereas on a hydrophilic surface ($\theta < 90°$) roughness has the opposite effect, decreasing θ toward 0°. Although the Wenzel equation is valid when the liquid droplet enters the valleys and completely wets the surface topography, the Cassie–Baxter model requires the presence of a liquid–vapor interface below the droplet [9]. At constant surface roughness, the surface chemistry can be designed to have the contact angle behavior go from the Wenzel regime to the Cassie–Baxter regime.

We have developed a simple, evaporation-driven procedure to deposit fractal SH coatings on arbitrary surfaces. It is derived from our earlier work on low-temperature/low-pressure aerogel coatings [10]. In this process, surface derivatization of silica sols with fluoroalkyl [11] groups causes drying shrinkage to be reversible. Springback at the final stage of drying results in a hierarchical fractal surface decorated with hydrophobic ligands. The advantage of our approach relative to many others is that SH surfaces form by (evaporation-induced) reassembly from a very low viscosity sol under standard laboratory conditions. This makes our procedure amenable to coating small features and virtually any kind of substrate. Applied to plastic, glass, metal, and silicon substrates and textiles, our SH coatings are optically transparent with contact angles exceeding 155°. In addition, we have developed a lithographic technique enabling optical adjustment of the water contact angle from 170° to <10°.

Although scanning electron microscopy (SEM) and atomic force microscopy (AFM) have been used routinely to image SH surfaces in air, a non-invasive technique such as X-ray or neutron scattering is required to study the buried water–SH film interface. Neutrons are particularly useful for such a study, because of their large penetration depth, isotopic sensitivity, and ability to contrast match portions of the system. NR has been used to study buried thin films and their interfaces [12–14]; it provides information about the scattering-length density, thickness, and interfacial roughness of different layers in a system.

Here, neutron reflectivity was used to understand the corrosive effect of saltwater on metals protected by SH films. UV/ozone treatment was used to vary the water contact angle and understand the resulting effect on the SH film interaction with D_2O.

3. Superhydrophobic film preparation

The SH coatings were made from a precursor solution containing mixed alkoxides 3,3,3-trifluoropropyl-trimethoxysilane (TFPTMOS) and tetramethyl orthosilicate (TMOS) using a variation of the aerogel thin film process reported by Prakash et al. [10]. The filtered sol was further diluted with ethanol and other solvents to obtain a final film thickness of ~5000 Å. Water contact angles consistently reached 155–160°, and angles up to 170° have been observed. The advancing and receding contact angle hysteresis is typically 5°. The effect of various process parameters on the SH behavior of the aerogel films is the topic of a future communication.

To prevent the potential dissolution of underivatized silica in the aqueous subphase [15,16] during the long acquisition times of NR (approximately 2–3 h), the D_2O subphase used in this study was made acidic by adding D_2SO_4 so as to make the final acid concentration 0.01 M (approximately equivalent to pH 2). No treatment to remove dissolved gases from D_2O was performed.

UV/ozone treatment was performed to photocalcine the organic ligands [17,18]. The time of exposure controlled the surface occupancy of the CH_3 and CF_3 groups, thereby adjusting the apparent contact angle, θ^{α}, while maintaining constant porosity, Φ_S, and roughness.

4. Neutron reflectivity

The reflectivity R of a surface is defined as the ratio of the number of particles (neutrons or photons) elastically and specularly scattered from the surface to the number of incident particles. When measured as a function of wave vector transfer, Q_z (defined below), the reflectivity curve contains information regarding the profile of the

Please cite this article in press as: P.M. Barkhudarov et al., Corrosion inhibition using superhydrophobic films, Corros. Sci. (2007), doi:10.1016/j.corsci.2007.10.005

in-plane average of the coherent scattering cross sections normal to the substrate. If one knows the chemical constituents of the investigated system and the concentration of a given atomic species at a particular depth, z, then the scattering-length density (SLD) distribution, $\beta(z)$, can be calculated from

$$\beta(z) = \frac{1}{\upsilon_m(z)} \sum_i^m b_i(z) \tag{1}$$

where b_i is the bound coherent scattering length of the ith of m atoms in the molecule with molecular volume v_m at location z. In the first Born approximation, the specular reflectivity, R, is related to the Fourier transform of the spatial derivative of the scattering-length density profile, $\mathrm{d}\beta/\mathrm{d}z$, by

$$R(Q_z) = R_{\mathrm{F}}(Q_z)\left|\frac{1}{\beta_{\mathrm{s}}}\int_{-\infty}^{+\infty}\frac{\mathrm{d}\beta(z)}{\mathrm{d}z}\exp(-iQ_z z)\mathrm{d}z\right|^2 \tag{2}$$

where R_{F} is the Fresnel reflectivity of the substrate and β_{s} is the substrate scattering-length density. Neutron reflectivity measurements were performed on the SPEAR beamline, a time-of-flight reflectometer, at the Manuel Lujan Jr. Neutron Scattering Center, Los Alamos National Laboratory (http://www.lansce.lanl.gov/lujan/instruments/SPEAR/index.html). The neutron beam is produced by the spallation of neutrons from a tungsten target using a pulsed beam (20 Hz) of 800 MeV protons. A partially coupled liquid hydrogen moderator at 20 K modifies the neutron energy spectrum. Neutrons with wavelengths of $\lambda = 2-16$ Å are selected by means of choppers and frame-overlap mirrors. The scalar value of momentum transfer vector Q_z is determined from $Q_z = 4\pi\sin(\alpha)/\lambda$ (where α is the angle of incidence measured from the sample surface and λ is the wavelength of the probe), and its range is covered by performing measurements at two angles of incidence, typically 0.5° and 2.5°. The beam footprint was 8 mm × 60 mm. The background limits the Q_z range over which reflectivity data can be collected; scattering from the subphase makes a significant contribution to the background. Hence, we designed a cell made of Maycor (Ceramic Products Inc, Palisades Park, NJ, containing $SiO_2/MgO/Al_2O_3/K_2O/B_2O_3/F$ in the weight ratio 46:17:16:10:7:4) to minimize the incoherent scattering from the cell, and the O-ring groove was machined to achieve a subphase reservoir depth of about 100–200 μm. A typical NR measurement took 2–3 h to accomplish, and therefore variations in sample structure were averaged over this period of time.

The reflectivity data is plotted on a semi-logarithmic scale versus Q_z, and the error bars represent the statistical uncertainty in the measurement.

The intensity of the specular reflectivity and the real-space SLD are related by the transformation given above. Because phase information is lost when collecting the specular reflectivity, as in most scattering experiments, and because of the non-linear nature of the inverse transformation, a unique solution to the problem cannot be obtained analytically. The reflectivity data were analyzed by a model-dependent Parratt formalism that requires a priori knowledge of the composition of the sample (SLD profile). In this model, the scattering-length density distribution $\beta(z)$ is described by a sequence of n slabs, each of constant scattering-length density. Two adjoining layers i and $i+1$ are connected by β_{int}, a sigmoidal function profile that describes the interfacial (chemical) roughness given by

$$\beta_{\mathrm{int}}(z) \propto erf\left(\frac{z - z_{\mathrm{mid}}}{\sigma}\right) \tag{3}$$

The error function is symmetric around z_{mid}, and so is the resulting interface profile. This is used as a convenient, well accepted model for interfacial roughness. We recognize that interfaces may not be symmetric, but because of the lack of a priori information from other experiments and theory, we are limited to the use of symmetric profiles to reduce the number of parameters in the fit and arrive at the simplest possible model.

The programs Parratt32 (http://www.hmi.de/bensc/instrumentation/instrumente/v6/refl/parratt_en.htm) and Motofit (http://motofit.sourcefourge.net) were used to analyze the reflectivity data and build models.

5. Results and discussion

We took reflectivity measurements of four samples to test films with different contact angles. The films were produced to represent the full range of possible contact angles. One was SH (>160°), one midrange (120°–130°), and one hydrophilic (<10°). The fourth sample was a control without any protective film.

The samples consisted of roughly 300–400 Å of aluminium sputtered onto a monocrystalline silicon bulk substrate. The aluminium layer thickness varied slightly between the different samples. The approximate roughness of the native silicon oxide on the surface of the silicon wafer was 3 Å. A ~5000 Å nano-porous film was applied to the aluminium surface using the technique described above. The sample surface was then submerged in 5 wt% NaCl D_2O solution. For each sample, NR measurements were taken immediately after immersion, and subsequently over periods of hours and days. The SPEAR neutron beam penetrated through the silicon bulk, reflected from all the buried interfaces, and finally the bulk D_2O layer on the bottom. This geometrical arrangement was used to avoid losses in neutron flux, as D_2O strongly absorbs neutrons, while silicon is nearly transparent to them. D_2O was used rather than H_2O, because the contrast in SLD between the nano-porous film and D_2O was larger than between the film and normal water (see Fig. 1). Q2

Given this sample composition, we based our models on the simplest possible six-layer arrangement. Fig. 2 shows a typical SLD profile of one of our samples. This one in particular is a sample with a SH (>160° contact angle) film on it. It is a snapshot of the average density distribution in the sample immediately after it was put in contact with the sal-

Please cite this article in press as: P.M. Barkhudarov et al., Corrosion inhibition using superhydrophobic films, Corros. Sci. (2007), doi:10.1016/j.corsci.2007.10.005

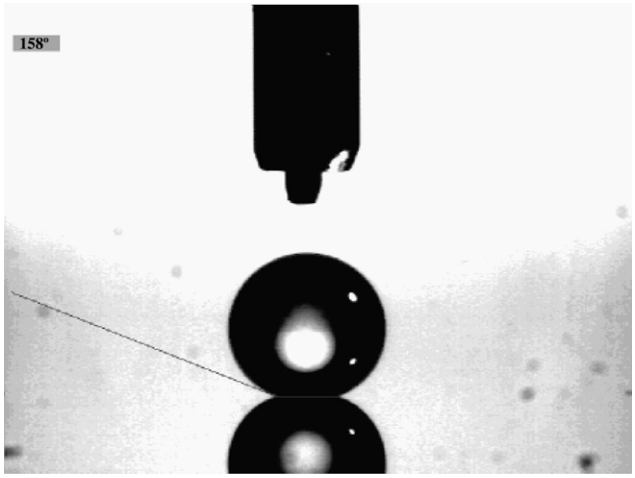

Fig. 1. Representative image of a sessile drop measurement of the water contact angle on a SH aerogel film showing a contact angle of 158 ± 2°.

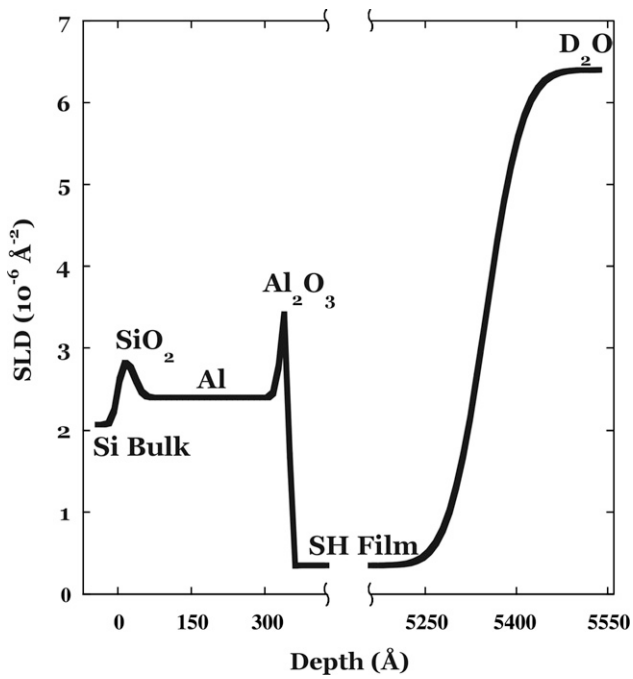

Fig. 2. An example of an SLD profile, consisting of an aluminium layer covered by a SH (>160° contact angle) film at time zero in contact with saline D_2O. During the fitting procedure, all the parameters were allowed to vary. The resulting reflectivity curve is given by the solid line in Fig. 3.

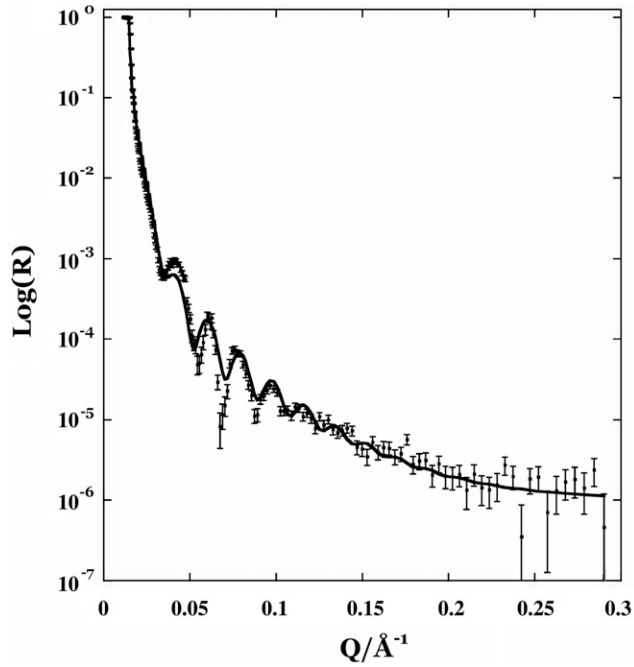

Fig. 3. Measured (data points with error bars) and calculated reflectivity (solid line) curves of the sample in Fig. 2. The spacing of the peaks is due primarily to the aluminium and oxide layers, and not due to the SH film.

ine D_2O, before any corrosion due to the water could have occurred. The layers from left to right (top to bottom in the actual sample environment) are: silicon, SiO_2, aluminium, Al_2O_3, SH film, and saline D_2O. Note that the SLDs of the silicon and aluminium oxide layers are lower than the known monocrystalline forms, implying that they have lower densities. Fig. 3 shows the measured and calculated reflectivity curves associated with the surface described by the density profile in Fig. 2. Due to the limited resolution of the SPEAR reflectometer (~3000 Å) and the rough film-D_2O interface, we do not observe the nano-porous film in the reflectivity curve. The errors of the fitted parameters were estimated by allowing χ^2 to vary by 5% and observing the deviation of the parameters from the optimum fit. The error margin for the aluminium thickness was about ±15 Å.

Using reflectivity data obtained for each sample at several points in time, we built reflectivity models to describe the SLD profile of the samples at each timestep. After obtaining parameters at time zero, only parameters relevant to water penetration and corrosion were allowed to vary in subsequent timesteps. For example, Fig. 4 shows the SLD profile change through time for the sample shown in Fig. 2.

It is clear from Fig. 4 that the corroded layer increased in thickness, causing the aluminium layer thickness to decrease accordingly. Note that the SLD of the corroded layer grew slightly over time, probably due to that layer no longer consisting purely of Al_2O_3. Fig. 5 summarizes the changes in aluminium layer thicknesses for all four samples. In order to avoid discrepancies caused by varying initial aluminium thicknesses in the different samples, we subtracted the initial aluminium thickness of each sample from all its data points, thus leaving only information about changes in thickness and ignoring irrelevant information about the absolute thicknesses of the layers. Fig. 6 shows the corresponding growth of the corroded layers over time (with a similar subtraction of initial oxide layer thicknesses). Fig. 6 does not include data from the unprotected aluminium sample, because the SLD of the corroded layer falls directly between that of aluminium and that of D_2O and is difficult to resolve.

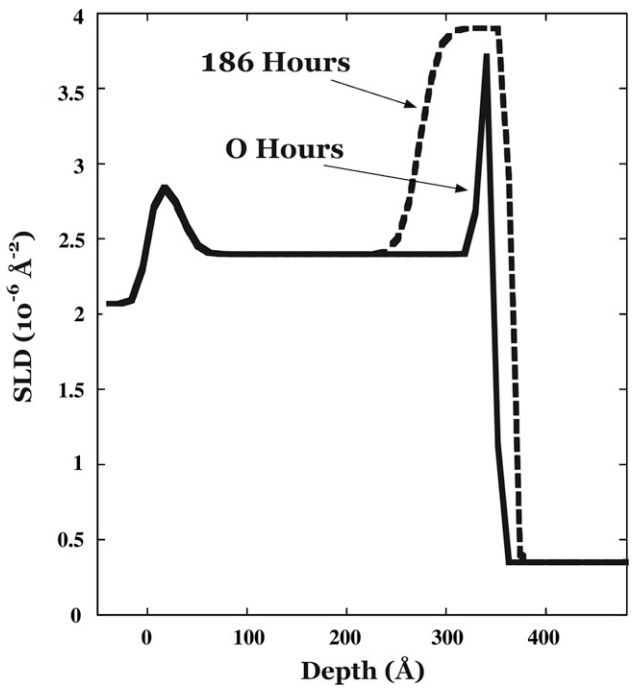

Fig. 4. The solid line is the same as in Fig. 1: the SH film-protected sample at time zero. The dashed line represents the SLD profile of the same sample after 186 h in the presence of saline D_2O. This represents a decrease in aluminium thickness and an increase in the thickness of the corroded layer. Note: only the part of the SLD profile relevant to corrosion is shown.

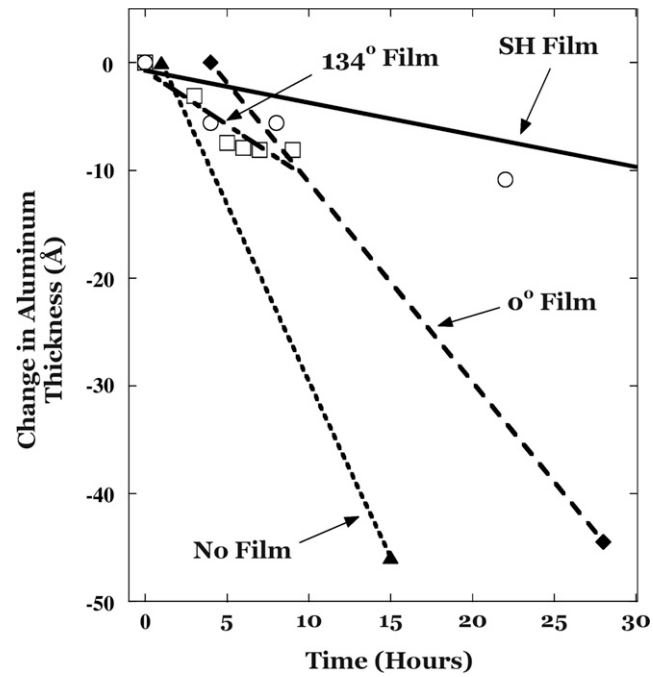

Fig. 5. The change in thickness of the aluminium layer versus time for samples protected by films of varying contact angle and a sample with only native Al_2O_3 layer (without protective film). At each data point, the initial aluminium layer thickness for that sample was subtracted in order to leave only information about changes in thickness. The solid and dashed lines represent linear fits of the aluminium layer thickness decrease. Note: the figure does not show all data points used to obtain the linear fit for the SH film sample, which was measured up to 186 h (This is why the SH line does not appear to be an accurate fit for the points shown in this figure).

Looking at the lines in Figs. 5 and 6, we can see that the aluminium protected by a SH film indeed corroded less than unprotected metal or metal covered with a less hydrophobic film. Taking the slopes of these linear fits, we find the average aluminium loss rates: ~0.3 Å/h for the SH-protected sample, ~1.01 Å/h for the midrange sample, ~1.85 Å/h for the zero degree film sample, and ~3.28 Å/h for the unprotected sample.

To conclude, the extreme case of a SH coating with a contact angle of >160° decreased the rate of corrosion roughly tenfold compared to the unprotected aluminium. This is a significant improvement, and with more cost effective SH film production, makes this a viable corrosion protection method. However, there was already an improvement when going from unprotected aluminium to aluminium with hydrophilic (0°) film on it. This is probably, because on the unprotected sample, Al_2O_3 gradually disintegrated or came off into the water, exposing more aluminium to corrosion. This dissolution could not occur in samples with protective films on them, as all new Al_2O_3 was trapped under the film, thereby providing an extra layer to block corrosive elements. More importantly, making the protective layer superhydrophobic rather than hydrophilic slowed corrosion by a further factor of six.

We must note that this measurement technique could not tell us whether or not pitting corrosion was occurring. If pitting corrosion were occurring, we would expect the SLD of the corroded layer to increase, since the pits in the layer would fill with D_2O. We do observe a slight increase in SLD in that layer (as shown in Fig. 4), but this cannot be unambiguously resolved.

In a previous paper investigating the properties of nano-porous films by Doshi et al. [19], it was shown that water penetrated a hydrophilic (0° contact angle) film completely, while not penetrating a 160° film at all. For 100° film, an intermediate water penetration was observed (5–10% less than the 0° film). We can conclude that the SH film used in our research indeed prevented (or minimized) water penetration to the metal surface below, and therefore resulted in greatly slowed corrosion. We could not directly observe water penetration in our measurements, because the films used (~5000 Å) were outside the resolution of the SPEAR reflectometer. Given, from the previous paper, that 100° and 0° films experience a high degree of water penetration, we can postulate that their performance as corrosion inhibitors would also be similar. Since the sample protected by a 134° film in our research experienced a significantly slower rate of corrosion than the 0° protected one, we make a further postulate that there is a contact angle threshold in between 100° and 134° at which water penetration begins to decrease more rapidly, and the films perform increasingly better as corrosion inhibitors. The nature of this threshold and the behavior of the nano-porous films near this point will be the subject of further study, to find the right balance of contact angle and corrosion protection.

Please cite this article in press as: P.M. Barkhudarov et al., Corrosion inhibition using superhydrophobic films, Corros. Sci. (2007), doi:10.1016/j.corsci.2007.10.005

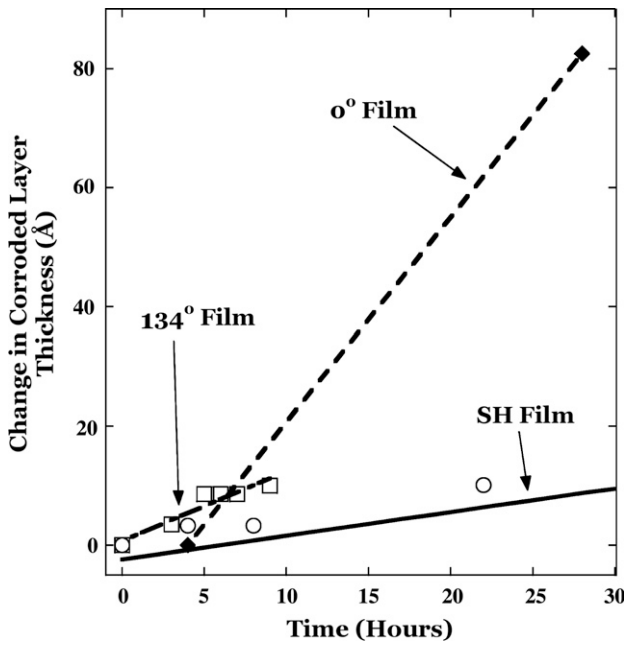

Fig. 6. The change in thickness of the corroded aluminium layer versus time for samples protected by films of varying contact angle. Similarly to Fig. 5, at each data point the initial native oxide layer thickness for that sample was subtracted to leave only information about thickness changes. Again, not all data points for the SH sample are shown. The unprotected aluminium sample is not shown here, as its oxide layer could not be resolved.

Acknowledgements

We acknowledge the support of the Los Alamos Neutron Science Center at the Los Alamos National Laboratory in providing the neutron research facility used in this work. The Los Alamos Neutron Science Center and the Los Alamos National Laboratory are funded by the US Department of Energy under Contract W-7405-ENG-36.

References

[1] W. Barthlott, C. Neinhuis, Planta (Heidelberg) 202 (1997) 1.
[2] C. Neinhuis, W. Barthlott, Ann. Bot. (London) 79 (1997) 667.
[3] K. Koch, C. Neinhuis, H.J. Ensikat, W. Barthlott, J. Exp. Bot. 55 (2004) 711.
[4] A.B.D. Cassie, Discuss. Faraday Soc. 3 (1948) 11.
[5] A.B.D. Cassie, S. Baxter, Trans. Faraday Soc. 40 (1944) 546.
[6] B. He, N.A. Patankar, J. Lee, Langmuir 19 (2003) 4999.
[7] S. Herminghaus, Europhys. Lett. 52 (2000) 165.
[8] R.N. Wenzel, Ind. Eng. Chem. 28 (1936) 988.
[9] J. Bico, C. Marzolin, D. Quere, Europhys. Lett. 47 (1999) 220.
[10] S.S. Prakash, C.J. Brinker, A.J. Hurd, S.M. Rao, Nature 374 (1995) 439. Q3
[11] A. Roig, E. Molins, E. Rodriguez, S. Martinez, M. Moreno-Manas, A. Vallribera, Chem. Commun. (2004) 2316.
[12] G. Fragneto-Cusani, J. Phys. Condens. Matter 13 (2001) 4973.
[13] S. Krueger, Curr. Opin. Coll. Interf. Sci. 6 (2001) 111.
[14] W.L. Wu, W.J. Orts, C.J. Majkrzak, D.L. Hunston, Poly. Eng. Sci. 35 (1995) 1000.
[15] R.K. Iler, The Chemistry of Silica, Wiley, New York, 1979.
[16] C.J. Brinker, G.W. Scherer, Sol–Gel Science: The Physics and Chemistry of Sol–Gel Processing, Academic Press, San Diego, CA, 1990.
[17] T. Clark, J.D. Ruiz, H.Y. Fan, C.J. Brinker, B.I. Swanson, A.N. Parikh, Chem. Mater. 12 (2000) 3879.
[18] A.M. Dattelbaum, M.L. Amweg, J.D. Ruiz, L.E. Ecke, A.P. Shreve, A.N. Parikh, Mater. Res. Soc. Symp. Proc. 788 (2003) 371.
[19] Dhaval A. Doshi, Pratik B. Shah, Seema Singh, Eric D. Branson, Anthony P. Malanoski, Erik B. Watkins, Jaroslaw Majewski, Frank von Swol, C.J. Brinker, Langmuir 21 (2005) 7805.